




## Phononic hybrid-order topology in semihydrogenated graphene

Wangping Liu <sup>\*</sup>, Zhong-Ke Ding <sup>\*</sup>, Nannan Luo, Jiang Zeng, Li-Ming Tang, and Ke-Qiu Chen <sup>†</sup>  
*Department of Applied Physics, School of Physics and Electronics, Hunan University, Changsha 410082, China*



(Received 12 January 2024; accepted 28 February 2024; published 18 March 2024)

In recent years, first-order and second-order topological phonons have been discovered in crystalline materials, which has aroused great interest. In the present work, through symmetry analysis and bulk polarization calculation, we demonstrate that semihydrogenated graphene (i.e., graphone) is an ideal platform intrinsically possessing hybrid-order (first-order and second-order) phonon topology. Based on the acoustic sum rule correction of the phonon tight-binding Hamiltonian, we show that the first-order optical and acoustic topological phonon edge states as well as second-order topological phonon corner states can coexist in graphone. Interestingly, the twofold degeneracy of topological acoustic phonon edge modes in graphene is eliminated due to spatial inversion breaking in graphone. In addition, there are three topological corner states within the wide gap of the phonon spectrum of the zigzag-edged nanodisk. Our results not only show hybrid-order topological phonon properties in graphone but also pave the way for a more complete understanding of topological phonons in other crystalline materials.

DOI: [10.1103/PhysRevB.109.115422](https://doi.org/10.1103/PhysRevB.109.115422)

### I. INTRODUCTION

The concept of topology has developed rapidly since the concept was introduced to the field of condensed matter physics. With the continuous advancement of topological theory, the study of topological phenomena is not limited to electronic systems [1–3]. The exploration of topological states has progressively extended to include photonic systems [4,5], as well as embracing phononic [6–13] and acoustic systems [14–19]. The signatures of topological phonons have been confirmed through experimental observation [20,21]. Crystalline materials contain various types of topological optical phonons, such as Dirac phonons [22–26], Weyl phonons [27–31], and nodal phonons [32–36]. Additionally, the topology of the acoustic triply degenerate point has been discussed [37,38], and topological acoustic phonon edge modes have been predicted in graphene [39]. In contrast to the phononic first-order topology, where the edge states appear at  $(d - n)$ -dimensional boundaries ( $n = 1, d > 1$ ) of the  $d$ -dimensional system, two-dimensional crystalline materials with phononic second-order topology [40–45] host topological states localized at zero-dimensional corners ( $n = 2, d = 2$ ).

In graphene, the twofold-degenerate topological acoustic phonon edge modes become nondegenerate by isotope doping [39], and the phononic second-order topological states in the  $z$  direction have been found through nitrogen doping [43]. Therefore, two-dimensional crystalline material based on graphene can be a promising candidate with rich topological phonon states. We intend to employ a more feasible approach than carbon isotope doping to break the space inversion symmetry of graphene, thereby exploring topological acoustic phonon edge modes in crystalline ma-

terials with intrinsic space inversion symmetry breaking. Moreover, we desire to obtain phononic second-order topological states in the crystalline material without the constraint that the lattice vibrations need to be decoupled in the  $z$  direction. Semihydrogenated graphene (i.e., graphone) has been reported in theoretical calculations and experimental synthesis [46–50], respectively, with spatial inversion symmetry breaking. In nanoelectronics and spintronics, graphone demonstrates significant applications [47], but deep exploration of the phononic topology of graphone is rarely reported.

In this work, through symmetry analysis and bulk polarization calculation, we discover that graphone exhibits phononic hybrid-order topology containing first- and second-order topological phonon states. By constructing the phonon tight-binding Hamiltonian for graphone nanoribbons, we reveal that the phononic first-order topology consists of topological optical and acoustic phonon edge states. The topological acoustic phonon edge states are localized at the boundaries of the zigzag graphone nanoribbons. Interestingly, unlike the twofold-degenerate topological acoustic phonon modes in graphene [39], the breaking of spatial inversion symmetry in graphone, induced by semihydrogenation, eliminates the degeneracy of the two topological acoustic phonon modes. Topological optical phonon edge states are also found in the graphone nanoribbons. In addition, we construct the tight-binding Hamiltonian for graphone nanodisks and find that the topological phonon corner and edge states exist in the armchair-edged graphone nanodisk. The phonon corner and edge states show robustness to defects in the nanodisk. Notably, the wide gap in the range of 40–70 THz of the zigzag-edged nanodisk phonon spectrum exclusively harbors three corner states. The results mentioned above are based on the phonon tight-binding Hamiltonian satisfying the acoustic sum rule (ASR) [39]. Our further analysis indicates that the ASR correction has a non-negligible impact on the topological state within the gap. Our results show that there is phononic

<sup>\*</sup>These authors contributed equally to this work.

<sup>†</sup>Author to whom correspondence should be addressed: keqiuchen@hnu.edu.cn

hybrid-order topology in graphone, making it an ideal platform for studying topological phonons.

## II. COMPUTATION DETAILS

The first-principles calculations were performed by using the Vienna *Ab initio* Simulation Package (VASP) [51,52] based on density functional theory (DFT) [53,54], and a  $\Gamma$ -centered Monkhorst-Pack [55]  $k$ -point grid was adopted for sampling in Brillouin zone. We used the generalized gradient approximation (GGA) with the Perdew-Burke-Ernzerhof (PBE) exchange-correlation functional [56]. The convergence criteria were set to  $1 \times 10^{-5}$  eV for energy and  $1 \times 10^{-3}$  eV/Å for force. The plane-wave energy cutoff was set to 520 eV, and a magnetic moment of about 1  $\mu$ B per unhydrogenated C atom. The force constants of bulk structures were calculated using the finite displacement method combined with the PHONOPY software package [57]. A supercell of  $7 \times 7 \times 1$  was used to calculate bulk force constants. The parameters from the bulk force constants were employed to construct the tight-binding Hamiltonian. A vacuum layer of 20 Å was applied along the  $z$  direction to eliminate spurious interaction between neighboring layers in our calculations.

## III. STRUCTURE AND PHONON SPECTRUM

The structure of graphone is shown in Fig. 1(a); the white and gray balls represent H and C atoms, respectively. The upper part of Fig. 1(a) shows a top view of the structure, while the lower part shows a side view. The green rhombic area represents the unit cell, containing two C atoms and one H atom, where one of the C atoms adsorbs one H atom. The optimized lattice constant for graphone is 2.55 Å. As half of the C atoms have adsorbed H atoms, the  $x$  and  $y$  coordinates of these C atoms and the corresponding H atoms are identical, while the  $z$  coordinates differ. The C atoms in graphone form the buckled structure due to their deviation from the perfectly planar structure of graphene. In graphone, half of the C atoms exhibit  $sp^2$  hybridization, while the remaining half display  $sp^3$  hybridization.

In terms of symmetry, graphone belongs to space group  $P3m1$  (no. 156), whereas the space group for pristine graphene is  $P6/mmm$  (no. 191). The symmetry of graphone is reduced from the  $C_6$  rotation symmetry present in graphene to  $C_3$ . The spatial inversion symmetry of graphone is intrinsically broken. The Wyckoff positions are a set of points in the lattice that remain invariant under symmetry operations of the lattice space group. A Wyckoff position is typically denoted by a combination of a number and a lowercase letter. The number represents the multiplicity of each Wyckoff position, indicating how many atoms each Wyckoff position can accommodate. The letter denotes the Wyckoff letter, typically starting from the letter “a” and arranged in order of increasing multiplicity in alphabetical order. In Fig. 1(a) we mark three Wyckoff positions (1a, 1b, 1c) using various symbols, where the 1a, 1b, and 1c are represented by a red circle, a purple hexagonal star, and a yellow triangle, respectively.

The global band gap means that there are no phonon states in the entire Brillouin zone (BZ) within the frequency range corresponding to the band gap. However, the local band gap only does not exist phonon states within the band-gap fre-

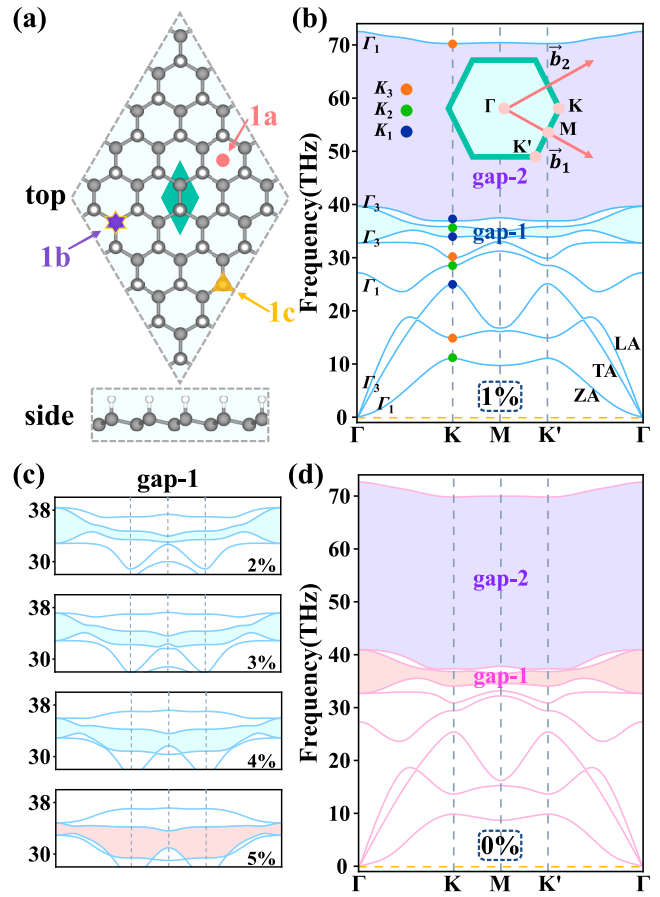


FIG. 1. The lattice structure of graphone and corresponding phonon spectra under strains. (a) Structure of graphone. The top view is presented in the upper part, while the side view is in the lower part. White and gray balls represent H and C atoms, respectively. The green rhombus represents the unit cell. Three Wyckoff positions are marked by a red circle (1a), a purple hexagonal star (1b), and a yellow triangle (1c), respectively. (b) The phonon spectrum of graphone under 1% strain. The little group representation at  $\Gamma$  and K in the Brillouin zone (BZ) is denoted by  $\Gamma_n$  and  $K_n$ . In the inset of (b), the regular hexagon represents the first BZ, where the high-symmetry points and basis vectors are marked by pink circles and red arrows, respectively. The light-blue area and the light-purple area represent gap 1 and gap 2, respectively. (c) Gap 1 of the graphone phonon spectrum under tensile strains of 2%–5%. The light-blue area indicates that gap 1 is local, while the light-red area signifies gap 1 is global. (d) Same as (b) but without strain.

quency range at some  $k$  points in the BZ, and there may be phonon states at other  $k$  points. In Fig. 1(d) the phonon spectrum of graphone features band gaps that can be categorized into two types based on whether they are global band gaps. We focus on the topology of the global band gaps. The graphone phonon spectrum exhibits two global band gaps, each referred to as gap 1 and gap 2. Gap 1 spans a frequency range of 35.5–36.4 THz, while gap 2 encompasses a frequency range of 40.9–69.8 THz. Constrained by the experimental conditions of material synthesis, the strain may be present in synthesized two-dimensional materials. Figure 1(b) illustrates the phonon spectrum of graphone under 1% tensile strain, and Fig. 1(c) showcases gap 1 under applied tensile strains of 2%–5%. It

is crucial to note that the strains we apply do not transform the symmetry of the structures. In Figs. 1(b)–1(d), both the light-red and light-blue areas represent gap 1. The light-red shading signifies the presence of a global band gap, while the light-blue area indicates a local band gap. Interestingly, under strains ranging from 1% to 4%, gap 1 is not global. In Sec. IV we demonstrate that gap 1 is topologically trivial while the gap 2 is topologically nontrivial. To better concentrate on the topologically protected gap, we shift our focus to the graphone under 1% tensile strain and gap 2.

In Fig. 1(b), revealing gap 2 in the phonon spectrum between 40 and 70 THz, the phonon spectrum of graphone is divided into two parts by gap 2. In the long-wavelength limit, the acoustic phonon modes of two-dimensional materials can be categorized into LA (longitudinal acoustic) mode, TA (transverse acoustic) mode, and ZA (out-of-plane) mode. The LA, TA, and ZA modes of graphone are labeled in Fig. 1(b). The  $\Gamma_n$  ( $n = 1, 3$ ) and  $K_n$  ( $n = 1, 2, 3$ ) in Fig. 1(b) represent little group representations at  $\Gamma$  and K points, respectively. The blue, green, and orange dots represent the three representations  $K_1$ ,  $K_2$ , and  $K_3$ , respectively. In the inset of Fig. 1(b), the green hexagonal area represents the first BZ of graphone, the pink dots denote high-symmetry points within the BZ, and the red arrows  $\vec{b}_1$  and  $\vec{b}_2$  indicate the basis vectors in momentum space.

#### IV. TOPOLOGICAL PROPERTIES

The diverse degrees of freedom within the electronic system, including charge, spin, and valley, facilitate the manipulation of electrons by applying an external field [58,59]. Phonons, as a kind of elementary excitation, are the main thermal carriers, extensively participating in various physical processes and interacting with other carriers [60–62], playing a critical role in thermoelectrics [63]. In contrast to electronic systems, phononic transport is not constrained by the Fermi level, and theoretically, all phononic modes contribute to the thermal transport processes. Nevertheless, in the manipulation degrees of freedom, phonons have fewer degrees of freedom than electrons. Consequently, manipulating phonons is not as straightforward as manipulating electrons. Although many efforts have been made in previous works on phonon transport [64–67], the manipulation of phonons remains challenging in most scenarios. The limited degrees of freedom in the phonon pose challenges in the design and application of thermal devices. Topological phonons as a novel phenomenon may become a new way to manipulate phonons [68].

We use group theory and topological quantum chemistry [69–73] methods to analyze the phononic second-order topology. In analogy with electronic systems, phonon bands can be categorized by referencing the concept of band gaps in semiconductors. We designate phonon bands below the gap as “occupied bands” and those above the gap as “unoccupied bands.” It is noteworthy that the terms “occupied” and “unoccupied” in this context do not describe the actual distribution of phonons. The first row of Table I presents the little group representations marked in Fig. 1(b), with the dimensions indicated in the parentheses. The second row lists the expectation values of corresponding representations under the  $C_3$  rotational symmetry operator.

TABLE I. The expectation values of the  $C_3$  rotational symmetry operator for the representations  $\Gamma_n$  ( $n = 1, 3$ ) and  $K_n$  ( $n = 1, 2, 3$ ).

Rep	$\Gamma_1(1)$	$\Gamma_3(2)$	$K_1(1)$	$K_2(1)$	$K_3(1)$
$C_3$	1	−1	1	$e^{i2\pi/3}$	$e^{-i2\pi/3}$

The bulk polarization  $p$  is a topological invariant that represents the displacement of the average phonon Wannier states from the center of the unit cell [15]. The bulk polarization can characterize the second-order topology [74], and the bulk polarization can be determined by extracting the expectation values of the symmetry operations at high-symmetry points within the Brillouin zone [75]. Under  $C_3$  rotational symmetry,  $p_i = p_j$ , where  $p_i$  and  $p_j$  represent the polarizations along the directions of  $\vec{b}_i$  and  $\vec{b}_j$ , respectively. The polarization can be determined using the expectation values corresponding to symmetry operators at high-symmetry points [75,76]. The bulk polarization of the  $n$ th band can be obtained from the following formula [15]:

$$(e)^{-i\pi(p_i)} = \prod_{n \in \text{occ}} \frac{\theta_n(\mathbf{K})}{\theta_n(\Gamma)}, \quad (1)$$

where  $\theta_n$  is the expectation value corresponding to the  $n$ th band at the high-symmetry point (K or  $\Gamma$ ) under the  $C_3$  rotational symmetry operator. According to the values listed in Table I, we can obtain the bulk polarization. In Fig. 1(d) the bulk polarization values ( $p_1, p_2$ ) for the occupied bands below gaps 1 and 2 are specifically (0,0) and  $(-2/3, -2/3)$ , respectively. The zero bulk polarization suggests that gap 1 is topologically trivial. In contrast, for gap 2 the fractional bulk polarization indicates that gap 2 is nontrivial. Therefore, topological phonon edge states may appear at the boundaries. In Sec. V, phononic topological edge states indeed emerge in the one-dimensional graphone nanoribbons along the zigzag and armchair boundaries within the frequency range of gap 2. Furthermore, we have identified topological phonon corner states and edge states in the phonon spectrum of zero-dimensional nanodisks. Gap 1 is not topologically protected, which is not global under 1%–4% biaxial tensile strains in Figs. 1(b) and 1(c). To explore the response of gap 1 to strain, biaxial tensile strains are applied to graphone, and gap 1 under  $-2\%$ – $5\%$  strains is presented in Fig. S1 of the Supplemental Material [77]. In the subsequent discussion we delve deeper into the reasons for the fractional bulk polarization through a symmetry analysis of graphone.

In the unit cell of graphone, the Wyckoff position 1b (0.333, 0.666,  $z$ ) is filled by a C atom. Simultaneously, the Wyckoff position 1c (0.666, 0.333,  $z$ ) is occupied by another C atom and one H atom. An elementary band representation (EBR) is a term used to describe a band representation that cannot be expressed as the sum of other band representations. A band representation can be expressed as a sum of EBR. The EBR can be expressed as  $R@w$ , where  $R$  represents the irreducible representation of the site symmetry group  $G_w$ , and  $w$  is the corresponding Wyckoff position. We categorize bands with close frequencies as a bandset, where bands within the same bandset do not intersect with those from other bandsets. The phonon spectrum in Fig. 1(b) can be divided into

TABLE II. The graphone phonon bands representations at high-symmetry points and the corresponding site representations with the Wyckoff positions. The first row lists Wyckoff positions with site symmetries inside the brackets. The second row gives the irreducible representations of the site-symmetry groups (IRSSG). The third and fourth are the little group representations at  $\Gamma$  and K points corresponding to the induced EBR, the dimensions of representations are in the brackets. The fifth row shows the notation of each bandset, the bands within a bandset do not intersect with bands outside the bandset.

Wyckoff	1b(3m)	1b(3m)	1b(3m)	1b(3m)	1c(3m)	1c(3m)
IRSSG	$A_1$	$E$	$A_1$	$E$	$E$	$A_1$
$\Gamma(0, 0, 0)$	$\Gamma_1(1)$	$\Gamma_3(2)$	$\Gamma_1(1)$	$\Gamma_3(2)$	$\Gamma_3(2)$	$\Gamma_1(1)$
$K(1/3, 1/3, 0)$	$K_2(1)$	$K_1(1) \oplus K_3(1)$	$K_2(1)$	$K_1(1) \oplus K_3(1)$	$K_1(1) \oplus K_2(1)$	$K_3(1)$
Bandset	S1		S2	S3	S4	S5

five bandsets, denoted as S1 to S5, in ascending order of frequency. Bandset S1 comprises only three acoustic phonon modes, while bandset S4 is composed of the second-highest and third-highest bands. Bandset S5 encompasses only the highest band.

The mechanical band representation [78] of bandsets can be expressed as the induced representations in corresponding local site representation. The mechanical band representation of S1 can be expressed as the sum of the induced representation of  $A_1$  and  $E$  at 1b, i.e.,  $A_1 @ 1b \oplus E @ 1b$ . The bandsets S2–S5 can be directly expressed as the induced representations from corresponding site representations  $A_1$ ,  $E$ ,  $E$ , and  $A_1$ , respectively. The band representations induced from the irreducible representations of the Wyckoff positions' symmetry group are listed in Table II. The mechanical band representation of bandsets S1 to S5 can be denoted as  $A_1 @ 1b \oplus E @ 1b$ ,  $A_1 @ 1b$ ,  $E @ 1b$ ,  $E @ 1c$ ,  $A_1 @ 1c$ , respectively. The mechanical band representation of S4 can be denoted as  $E @ 1c$ , where the Wyckoff position 1c has a multiplicity of only 1, which means it can accommodate only one atom. However, in graphone there is more than one atom at the Wyckoff position 1c in Fig. 1(a). The mismatch between the Wannier centers of phonons and the atomic positions in the bandset S4 (the bulk polarization of S4 is  $-2/3$ ) are what causes the non-trivial gap 2 between bandsets S4 and S5. Correspondingly, the mechanical band representation of bandset S3 is denoted as  $E @ 1b$ ; there is only one unhydrogenated C atom at the Wyckoff position 1b in Fig. 1(a). Unlike the mismatch in S4, there is no such mismatch in S3 (the bulk polarization of S3 is zero), making gap 1 between bandsets S3 and S4 trivial.

The preceding analysis primarily focuses on the topological optical phonon. Nevertheless, within the phonon transport, the acoustic phonon plays a vital role as well as the optical phonon. Hence, we also seek the exploration of the topological acoustic phonon. In the phononic system, frequencies of three acoustic phonon modes approach zero in the long-wavelength limit, and an acoustic triply degenerate point emerges at the  $\Gamma$  point. The topology of the acoustic triply degenerate point in graphene has been discussed in Ref. [38], and the corresponding topological acoustic phonon edge modes have been found in the graphene zigzag nanoribbon. Breaking the inversion symmetry of graphene can split the degenerate two acoustic phonon modes by isotope doping [39]. Therefore, while semihydrogenation of graphene will also break the inversion symmetry, the topological acoustic phonon edge modes will not vanish.

## V. OPTICAL AND ACOUSTIC PHONON EDGE STATES IN NANORIBBONS

In the top views of the zigzag and armchair nanoribbons in Figs. 2(a) and 2(b), the atoms in the middle part are not displayed. The periodic boundary condition and the open boundary condition are applied in the  $x$  and  $y$  direction, respectively. We employ four distinct colors to delineate the boundaries of zigzag and armchair nanoribbons. The upper and lower boundaries of the armchair nanoribbon are denoted by blue and orange, respectively, while the upper and lower boundaries of the zigzag nanoribbon are represented by green and pink, respectively. In Figs. 2(c) and 2(d), we additionally color-code the topological phonon edge states in the phonon spectrum; the edge states of each color are distributed at the boundaries of the same color. We also calculate the phonon spectrum of different widths of nanoribbons in the Supplemental Material [77].

In Fig. 2(c) we depict the corresponding phonon spectrum for the structure presented in Fig. 2(a). The blue and orange dashed lines in the plot signify the two topological optical phonon edge modes, distinctly visible in the inset of Fig. 2(c) and positioned away from the bulk states. The two topological phonon edge modes are respectively distributed along the upper and lower boundaries of the armchair nanoribbon. It is noteworthy that the mirror symmetry along the  $y$  direction of the armchair nanoribbon in Fig. 2(a) is broken, meaning the upper and lower boundaries are distinct. If the mirror symmetry of the armchair nanoribbon is preserved, the two topological optical phonon modes will completely degenerate, and both modes will be present on both upper and lower boundaries. The topological optical phonon edge mode in the graphone zigzag nanoribbon is marked by a pink line in Fig. 2(d), and the optical phonon edge states are distributed at the lower boundary of the graphone zigzag nanoribbon.

The multiplicity of the Wyckoff position 1c is 1, but there is one C and one H atom occupying the same Wyckoff position 1c in graphone. When multiple atoms occupy the Wyckoff position 1c at the boundaries of nanoribbons, the mismatch between Wannier centers of phonons and atomic positions occurs. This mismatch leads to the occurrence of the topological phonon edge state. Consequently, the exposure of the Wyckoff positions 1c at the boundary of the graphone open boundary system gives rise to the appearance of the topological optical phonon edge states. In Figs. 2(c) and 2(d), the phonon spectrum of armchair nanoribbons has two

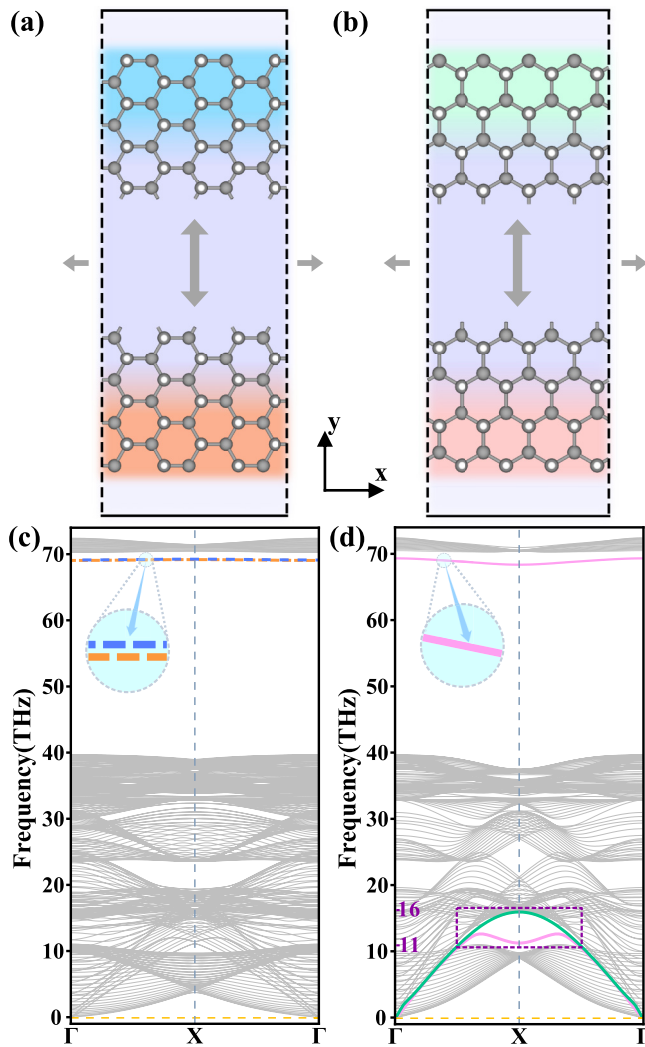


FIG. 2. Two types of graphane nanoribbons and corresponding phonon spectra. (a), (b) Top views of the graphane armchair and zigzag nanoribbons. The blue and orange areas respectively indicate the upper and lower boundaries of the armchair nanoribbon, while the green and pink areas represent the upper and lower boundaries of the zigzag nanoribbon, respectively. (c), (d) The phonon spectra respectively correspond to the structures in (a) and (b), with colored lines representing topological edge states. (c) The blue and orange dashed lines indicate topological optical phonon edge states localized at the upper and lower boundaries of the armchair nanoribbon, respectively. (d) The pink line in a high-frequency interval represents topological optical phonon edge states, localized at the lower boundary of the zigzag nanoribbon. In the local band gap in a low-frequency interval marked by the dark-magenta dashed-line box, the pink and green lines represent topological acoustic phonon edge states localized at the lower and upper boundaries, respectively. The high-symmetry points in reciprocal space as  $\Gamma$  (0, 0, 0) and X (0.5, 0, 0).

topological optical phonon edge modes, while the phonon spectrum of zigzag nanoribbons has only one topological optical phonon mode. The corresponding enlarged view of the topological optical phonon edge states in the zigzag nanoribbon is shown in the inset of Fig. 2(d). The discrepancy in the number of topological optical phonon edge modes in the

phonon spectra of zigzag and armchair nanoribbons can be attributed to the distinct occupation of atoms at the Wyckoff positions 1c along corresponding boundaries of nanoribbons. In the zigzag nanoribbon shown in Fig. 2(b), the topological optical phonon edge states are only distributed at the lower boundary, as the Wyckoff positions 1c are exposed solely at the lower outermost boundary; the Wyckoff positions 1c coexist at the upper and lower outermost boundaries of the armchair nanoribbon in Fig. 2(a). Therefore, the number of topological optical phonon edge modes in the armchair nanoribbon is twice that of the zigzag nanoribbon.

The topological acoustic phonon edge modes are distributed at the boundaries of the graphane zigzag nanoribbon. In Figs. 2(b) and 2(d), we illustrate the top view and phonon spectrum of the graphane zigzag nanoribbon. In the phonon spectrum of the graphane zigzag nanoribbon, two topological acoustic phonon edge modes are indeed observed in the local band gap ranging from 11 to 16 THz, framed by the dark-magenta dashed-line box in Fig. 2(d), marked by pink and green lines in Fig. 2(d). The pink and green lines represent the states localized at the lower and upper boundaries of the graphane zigzag nanoribbon, respectively.

In graphene, there are the twofold-degenerate topological acoustic phonon modes within the local band gap of the zigzag nanoribbon spectrum, and energies of topological acoustic phonon modes undergo a slight split following isotope doping [39]. In graphane, semihydrogenation results in the hydrogenation of one of the boundaries of the graphane zigzag nanoribbon. The two topological acoustic phonon edge modes are localized at the upper and lower boundaries, respectively, as shown in Fig. 2(b). Whether isotope doping or semihydrogenation is applied to graphene, both cases induce the breaking of spatial inversion symmetry, consequently eliminating the twofold degeneracy of topological acoustic phonon edge modes. The boundary at which the outermost carbon atoms in the zigzag nanoribbon is hydrogenated is called the hydrogenation boundary. In Fig. 2(b) the lower boundary of the zigzag nanoribbon is the hydrogenated boundary. However, the hydrogenated boundary of the graphane zigzag nanoribbon exhibits notable differences from the boundaries of the isotope-doped graphene zigzag nanoribbon. Therefore, in comparison to the situation of isotope doping in graphene [39], semihydrogenation induces significant alterations in the group velocity and frequency of the topological acoustic phonon edge mode at the hydrogenated boundary. The two topological acoustic phonon edge modes in the graphane zigzag nanoribbon correspond to the in-plane modes, while the out-of-plane mode is topologically trivial.

The local densities of states are shown in Fig. 3 for both graphane armchair and zigzag nanoribbons in Figs. 2(a) and 2(b), respectively. Figure 3 can be divided into upper and lower parts by a dashed blue line in the middle. The densities of states (DOS) are projected onto the armchair nanoribbon in the upper part, Arm-Nan represents the graphane armchair nanoribbon shown in Fig. 2(a), and the lower part contains the projected DOS of the zigzag nanoribbon. Correspondingly, Zig-Nan stands for the graphane zigzag nanoribbon in Fig. 2(b). Figure 3 can also be divided into three regions from left to right according to the different background colors. The blue part on the left represents the projection of the

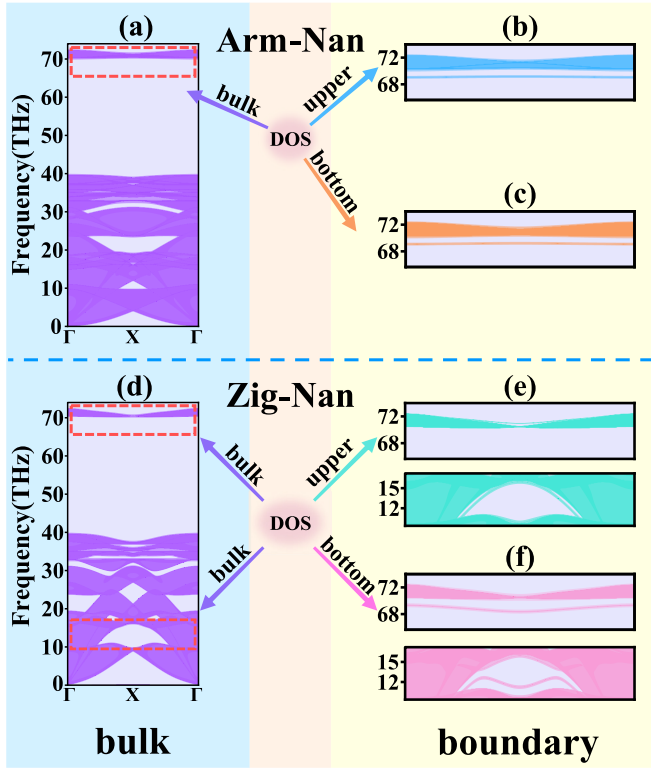


FIG. 3. Local density of states of the armchair and zigzag nanoribbons. Arm-Nan and Zig-Nan represent the graphone armchair and zigzag nanoribbons, respectively. (a)–(c) The density of states (DOS) projected onto the graphone armchair nanoribbon’s bulk (purple), lower boundary (orange), and upper boundary (blue), respectively, and in (b)–(c) DOS are only plotted corresponding to the frequency range of the dashed box in (a). (d)–(f) The density of states projected onto the graphone zigzag nanoribbon’s bulk (purple), lower boundary (pink), and upper boundary (green), respectively, and in (e)–(f) DOS are only plotted corresponding to the frequency range of the dashed boxes in (d).

DOS at bulk, and the light-yellow area on the right represents the projection of the DOS at the boundary. In Fig. 3(a) a high-frequency interval of DOS is marked with a red-dashed-line box, while the two red-dashed-line boxes in Fig. 3(d) mark the high-frequency interval and low-frequency interval of DOS, respectively. In Figs. 3(a)–3(c), the DOS is projected onto the graphone armchair nanoribbon’s bulk (purple), lower boundary (orange), and upper boundary (blue), respectively. The DOS is projected onto the graphone zigzag nanoribbon’s bulk (purple), lower boundary (pink), and upper boundary (green), respectively, in Figs. 3(d)–3(f). In Figs. 3(b)–3(c) and 3(e)–3(f) we do not plot the full DOS but only DOS in the frequency range corresponding to the red-dashed-line box in Figs. 3(a) and 3(b), respectively, because we are mainly concerned with topological phonon edge states in frequency ranges of dashed-line boxes.

By comparing the DOS in Figs. 3(b) and 3(c) with the red-dashed-line box in Fig. 3(a), it can be noted that there are indeed the topological phonon edge states distributed in the high-frequency interval within the global band gap of the graphone armchair nanoribbon. The topological phonon edge states of the armchair nanoribbon are localized at both the

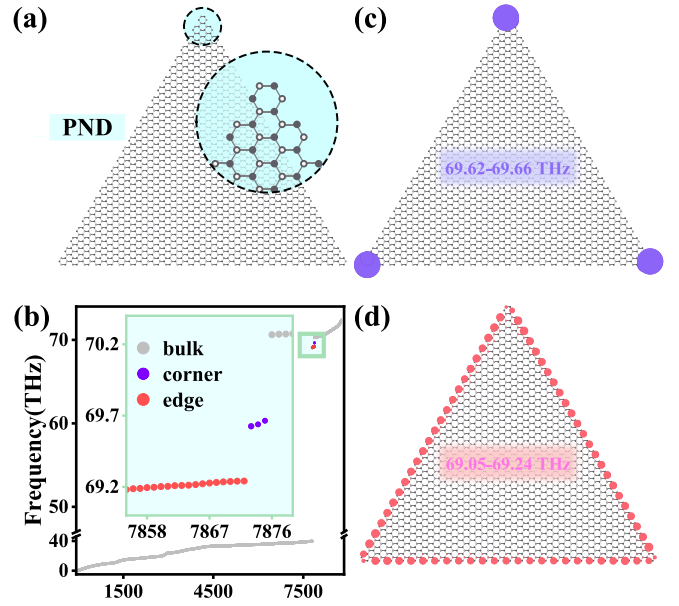


FIG. 4. Graphone perfect nanodisk and corresponding phonon spectrum, along with the distribution of the topological states in real space. (a) Top view of the graphone armchair-edged perfect nanodisk (PND). The white and gray circles represent the H and C atoms, respectively. The light-blue circular region on the right is an enlarged view of the top of the triangular nanodisk. (b) Phonon spectrum corresponding to the PND in (a). The inset in (b) includes part of the states within the small green box; gray, purple, and red dots represent bulk states, corner states, and edge states, respectively. (c), (d) Spatial distribution of the topological states in the PND, purple and red circles denote corner and edge states, respectively.

upper and lower boundaries. Correspondingly, in the comparison of DOS in Figs. 3(e) and 3(f) with the red dashed box in Fig. 3(d), it is evident that the topological phonon edge states in the high-frequency and low-frequency intervals do exist at the lower boundary of graphone zigzag nanoribbon.

## VI. PHONON TOPOLOGICAL STATES IN NANODISK

Similar to the higher-order topology of electronic systems [79–83], there is a higher-order bulk-boundary correspondence in two-dimensional crystalline materials with phononic second-order topology [40–45], i.e., there are topological phonon corner states at zero-dimensional corners. The non-trivial bulk polarization of gap 2 indicates the existence of phononic second-order topology in graphone. To explore phononic high-order topology, we construct triangular graphone nanodisks due to the  $C_3$  rotational symmetry of graphone, focusing on the topology within the nanodisks. In Fig. 4(a), the top view of the graphone triangular armchair-edged nanodisk, gray and white circles represent C atoms and H atoms, respectively, where the light-blue region on the right is a magnified view corresponding to the dashed circular area at the top of the triangular nanodisk structure.

We refer to the triangular nanodisk in Fig. 4(a) without defects as the perfect nanodisk (PND). The PND consists of 2925 atoms, with a side length of 10.8 Å. To focus on non-trivial phonon corner states, we present the nanodisk phonon

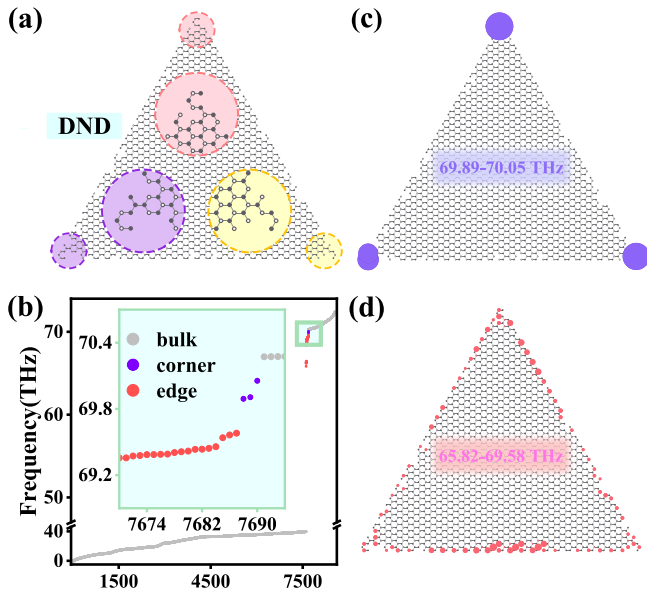


FIG. 5. Structure and phonon spectrum of the graphone defective nanodisk, along with the spatial distribution of topological states. (a) The top view of the defective nanodisk (DND). The three large circles inside the nanodisk correspond to the enlarged views that show the regions marked by the three small dashed circles, and the same color represents the corresponding relationship for each pair of circles. (b) Phonon spectrum corresponding to the DND in (a). The inset includes part states within the small green box in the gap, with red, purple, and gray dots representing edge states, corner states, and bulk states, respectively. (c), (d) Spatial distribution of the topological states within the DND, purple and red circles represent corner and edge states, respectively.

spectrum under 1% tensile strain in Fig. 4(b). Detailed phonon spectra of the nanodisk under other strain conditions can be found in the Supplemental Material [77]. Under the no-strain condition, a band gap emerges in the phonon spectrum of the nanodisk corresponding to the frequency range of gap 1 in the phonon spectrum in Fig. 1(c), encompassing phonon corner and edge states. The same situation occurs at 1% compressive strain. However, under 2% compressive strain and 1%–5% tensile strain conditions, in the nanodisk phonon spectrum, corresponding to the frequency range of gap 1 in the phonon spectrum of bulk graphone, either there is no gap or the gap is too small to accommodate any states. In the –2% to 5% strain conditions, there is a gap ranging from approximately 40 to 70 THz in the phonon spectrum of the nanodisk corresponding to the frequency range of gap 2 in the phonon spectrum of the bulk graphone, and the topological phonon corner or edge states are consistently present within the gap. Consequently, in the following content we discuss only the gap containing topological states in the phonon spectrum of the nanodisk.

In Figs. 4(b), 5(b), and 6(b) we adjusted the vertical axis scale to highlight the topologically nontrivial states. In Fig. 4(b) the small green box contains the topological states within the gap and several bulk states. The inset in Fig. 4(b) is an enlarged view of part of the area in the small green box in the gap, containing part bulk states and topological states, where the purple, red, and gray dots represent the corner, edge, and bulk states, respectively. The topologically

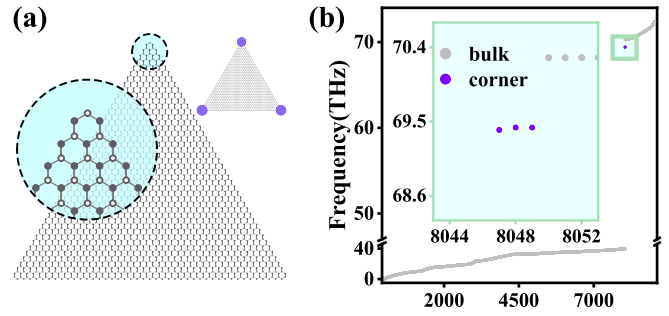


FIG. 6. The graphone zigzag-edged nanodisk and corresponding phonon spectrum. (a) The structure of the graphone triangular zigzag-edged nanodisk. The light-blue circular region on the left is the enlarged view of the top of the triangular nanodisk. The inset shows the spatial distribution of corner states denoted by purple circles in the nanodisk. (b) The phonon spectrum corresponds to the graphone nanodisk in (a). The inset represents an enlarged view of the small green box within the gap, with gray and purple dots representing bulk states and topological corner states, respectively.

nontrivial states of the PND are distributed in the gap of the phonon spectrum, spanning a frequency range of approximately 69.05–69.66 THz. Figure 4(c) illustrates the spatial distribution of the three topological phonon corner states represented by purple circles within the PND. Additionally, Fig. 4(d) presents the spatial distribution of the topological edge states, represented by the red circles. The mismatch between Wannier centers of phonons and atomic positions in graphone leads to the occurrence of phonon corner and edge states in the nanodisk, all of which are topologically protected.

Despite the persistent existence of the topological states under different strains in Fig. S2 of the Supplemental Material [77], to further validate the robustness of the topological states against defects, we construct the defective nanodisk (DND) by introducing random defects at the boundaries of the PND, the number of defects accounting for 10% of atoms at the boundaries. Figure 5(a) displays the top view of the DND. To clearly depict the corners of the DND, we employ three pairs of circles, each pair consisting of a large one and a small one. The same color represents the corresponding relationship for each pair of circles. The three large circles are the magnified views of the regions marked by the three small dashed circles.

Figure 5(b) illustrates the phonon spectrum of the DND; the frequency distribution of the topological phonon edge and corner states are between 65.80 and 69.50 THz, 69.90 THz and 70.05 THz, respectively. Following the introduction of defects, the frequencies of the topological states within the gap of the DND phonon spectrum vary markedly compared with the topological states of the PND in Fig. 4(b). The introduction of defects at the PND boundaries will cause both the disappearance of a portion of atoms at Wyckoff positions 1c at the PND boundaries and the appearance of new boundaries that contain atoms located at Wyckoff 1c positions. Subsequent to the introduction of defects, the disappearance of a part of the original topological edge states in the PND and the emergence of new edge states in the DND lead to significant changes in the frequency range of edge states in the gap. In the DND, topological phonon corner and edge states persist

within the gap and do not disappear. The inset in Fig. 5(b) provides a more detailed view of part of the area in the small green box. The average corner states and edge states of the DND are depicted in Figs. 5(c) and 5(d). Hence, when defects are introduced at the boundaries of the PND, the topological states demonstrate robustness and the capacity to withstand the effects of defects.

The discussion above regarding phononic second-order topology is established on the armchair-edged nanodisk. Within the gap of the phonon spectrum of the armchair-edged nanodisk, there are not only phonon corner states but also edge states. However, the coexistence of topological phonon corner and edge states in the same gap may hinder the application of corner states. In order to investigate the case that the gap in the phonon spectrum of the triangular nanodisk contains only three corner states, we construct the zigzag-edged nanodisk. The structure of the graphone triangular zigzag-edged nanodisk in Fig. 6(a) and the light-blue circle is the enlargement of the top of the structure, and the inset is the spatial distribution of topological corner states that are denoted by purple circles. The frequencies of the three topological corner states lie between the gap in the zigzag-edged nanodisk phonon spectrum in Fig. 6(b). In this configuration, the outermost boundaries consist of C atoms located at Wyckoff positions 1b, while only the three vertices of the triangular nanodisk contain H and C atoms situated at Wyckoff positions 1c. Consequently, in the inset of Fig. 6(b), the triangular zigzag-edged nanodisk manifests only three topological phonon corner states within the gap, with no presence of topological edge states. Compared to the gap in the phonon spectrum of the armchair-edged nanodisk that contains many edge and corner states in Fig. 4(b), the gap in the phonon spectrum of the zigzag-edged nanodisk is concise, containing only three topological corner states.

In the construction of the tight-binding Hamiltonian here, we take into account the correction of Hamiltonian by the acoustic sum rule (ASR) [39], ensuring that the frequencies of acoustic phonon modes approach zero in the long-wavelength limit. It is worth underscoring that the correction of ASR not only significantly affects the acoustic phonon modes of the open boundary system but also has a considerable effect on the topological optical phonon modes. We construct tight-binding Hamiltonians of the graphone nanoribbon and nanodisk, which do not satisfy ASR, and the corresponding phonon spectra are shown in Fig. S3 of the Supplemental Material [77]. For the graphone nanoribbons, ignoring the correction of ASR would lead to the disappearance of topological optical and acoustic phonon edge states marked within the local band gap or global band gap with colored lines in Figs. 2(c) and 2(d). Compared with the case that the Hamiltonian satisfies ASR, the topological edge states or corner states within the gap of the phonon spectrum of the nanodisk disappear when the correction of ASR is neglected. Hence, when constructing the phonon Hamiltonian of an open boundary system, the correction of boundary atoms by ASR cannot be overlooked. It is worth noting that the system we studied is a freestanding graphone. In this case the phonon Hamiltonian of the system satisfies ASR, where dangling bonds at the boundaries have no interaction with the external environment. If dangling bonds interact with the outside, such as the sample

on the substrate, the interaction between dangling bonds and the substrate is worthy of further study and discussion.

## VII. CONCLUSION

By symmetry analysis and bulk polarization calculation, we predict that semihydrogenated graphene (i.e., graphone) hosts phononic hybrid-order topology containing first-order topological phonon edge states and second-order topological phonon corner states. The graphone phonon spectrum under no strain exhibits two global band gaps, gaps 1 and 2. We find that the bulk polarization for gap 1 is zero, while the bulk polarization for gap 2 is  $-2/3$ . A zero value for bulk polarization signifies gap 1 is trivial. The fractional bulk polarization indicates that gap 2 is topologically nontrivial. By constructing the phonon tight-binding Hamiltonians and diagonalizing them, we obtain the corresponding phonon spectra for nanoribbons and nanodisks. For the one-dimensional graphone nanoribbons, the topological optical phonon edge states are localized at the boundaries of zigzag and armchair nanoribbons. The topological acoustic phonon edge states are distributed at the boundaries of the zigzag nanoribbon. The two topological acoustic phonon edge modes are situated in a local band gap of the zigzag nanoribbon phonon spectrum. Compared with the twofold-degenerate topological acoustic phonon edge modes in graphene, the two topological acoustic edge modes of graphone are nondegenerate, since semihydrogenation breaks the spatial inversion symmetry. For the zero-dimensional graphone nanodisks, topological phonon corner states and edge states emerge in the armchair-edged nanodisk, and we find that the gap ranging from 40 to 70 THz in the zigzag-edged nanodisk phonon spectrum only contains three topological phonon corner states. Through symmetry analysis we discover that the topological optical phonon states of nanoribbons and topological corner states of nanodisk arise due to the mismatch between the phonon Wannier centers and atomic positions at Wyckoff positions 1c. Owing to topological protection, the phonon corner and edge states exhibit robustness against defects in the nanodisk. The above results are based on the acoustic sum rule correction of the phonon Hamiltonian. Our further exploration shows that the correction of ASR is indispensable for the phononic system. The correction of ASR not only plays a crucial role for acoustic phonons, ensuring that frequencies of acoustic phonons approach zero in the long-wave limit, but also for topological optical phonons. When the correction of the phonon Hamiltonian by ASR is ignored, the topological states distributed in the gap of the graphone open boundary system phonon spectrum may vanish. The coexistence of the first-order topology of both optical and acoustic phonons, along with phononic second-order topology in graphone, illustrates that graphone is an ideal candidate crystalline material for studying phononic topology. Our results contribute to enhancing our comprehension of the phononic hybrid-order topology in the crystalline material.

## ACKNOWLEDGMENTS

This work was financially supported by the National Key Research and Development Program of Ministry of Science and Technology (2022YFA1402504) and by the National Natural Science Foundation of China (Grant No. 12374040).



- [1] D. Hsieh, Y. Xia, D. Qian, L. Wray, J. Dil, F. Meier, J. Osterwalder, L. Patthey, J. Checkelsky, N. P. Ong *et al.*, A tunable topological insulator in the spin helical Dirac transport regime, *Nature (London)* **460**, 1101 (2009).
- [2] M. Z. Hasan and C. L. Kane, Colloquium: Topological insulators, *Rev. Mod. Phys.* **82**, 3045 (2010).
- [3] D. Xiao, M.-C. Chang, and Q. Niu, Berry phase effects on electronic properties, *Rev. Mod. Phys.* **82**, 1959 (2010).
- [4] S. Mittal, V. V. Orre, G. Zhu, M. A. Gorkach, A. Poddubny, and M. Hafezi, Photonic quadrupole topological phases, *Nat. Photon.* **13**, 692 (2019).
- [5] T. Ozawa, H. M. Price, A. Amo, N. Goldman, M. Hafezi, L. Lu, M. C. Rechtsman, D. Schuster, J. Simon, O. Zilberberg, and I. Carusotto, Topological photonics, *Rev. Mod. Phys.* **91**, 015006 (2019).
- [6] C. Strohm, G. L. J. A. Rikken, and P. Wyder, Phenomenological evidence for the phonon Hall effect, *Phys. Rev. Lett.* **95**, 155901 (2005).
- [7] L. Zhang, J. Ren, J.-S. Wang, and B. Li, Topological nature of the phonon Hall effect, *Phys. Rev. Lett.* **105**, 225901 (2010).
- [8] P. Wang, L. Lu, and K. Bertoldi, Topological phononic crystals with one-way elastic edge waves, *Phys. Rev. Lett.* **115**, 104302 (2015).
- [9] Y. Liu, C.-S. Lian, Y. Li, Y. Xu, and W. Duan, Pseudospins and topological effects of phonons in a Kekulé lattice, *Phys. Rev. Lett.* **119**, 255901 (2017).
- [10] Y. Long, J. Ren, and H. Chen, Unsupervised manifold clustering of topological phononics, *Phys. Rev. Lett.* **124**, 185501 (2020).
- [11] Y. Liu, X. Chen, and Y. Xu, Topological phononics: From fundamental models to real materials, *Adv. Funct. Mater.* **30**, 1904784 (2020).
- [12] J. Li, J. Liu, S. A. Baronett, M. Liu, L. Wang, R. Li, Y. Chen, D. Li, Q. Zhu, and X.-Q. Chen, Computation and data driven discovery of topological phononic materials, *Nat. Commun.* **12**, 1204 (2021).
- [13] M. Gutierrez-Amigo, M. G. Vergniory, I. Errea, and J. L. Mañes, Topological phonon analysis of the two-dimensional buckled honeycomb lattice: An application to real materials, *Phys. Rev. B* **107**, 144307 (2023).
- [14] Z.-G. Chen, C. Xu, R. Al Jahdali, J. Mei, and Y. Wu, Corner states in a second-order acoustic topological insulator as bound states in the continuum, *Phys. Rev. B* **100**, 075120 (2019).
- [15] X. Ni, M. Weiner, A. Alu, and A. B. Khanikaev, Observation of higher-order topological acoustic states protected by generalized chiral symmetry, *Nat. Mater.* **18**, 113 (2019).
- [16] Z. Zhang, B. Hu, F. Liu, Y. Cheng, X. Liu, and J. Christensen, Pseudospin induced topological corner state at intersecting sonic lattices, *Phys. Rev. B* **101**, 220102(R) (2020).
- [17] Z.-Z. Yang, X. Li, Y.-Y. Peng, X.-Y. Zou, and J.-C. Cheng, Helical higher-order topological states in an acoustic crystalline insulator, *Phys. Rev. Lett.* **125**, 255502 (2020).
- [18] Y. Yang, J. Lu, M. Yan, X. Huang, W. Deng, and Z. Liu, Hybrid-order topological insulators in a phononic crystal, *Phys. Rev. Lett.* **126**, 156801 (2021).
- [19] Q. Wei, X. Zhang, W. Deng, J. Lu, X. Huang, M. Yan, G. Chen, Z. Liu, and S. Jia, Higher-order topological semimetal in acoustic crystals, *Nat. Mater.* **20**, 812 (2021).
- [20] Z. Jin, B. Hu, Y. Liu, Y. Li, T. Zhang, K. Iida, K. Kamazawa, A. I. Kolesnikov, M. B. Stone, X. Zhang, H. Chen, Y. Wang, I. A. Zaliznyak, J. M. Tranquada, C. Fang, and Y. Li, Chern numbers of topological phonon band crossing determined with inelastic neutron scattering, *Phys. Rev. B* **106**, 224304 (2022).
- [21] J. Li, J. Li, J. Tang, Z. Tao, S. Xue, J. Liu, H. Peng, X.-Q. Chen, J. Guo, and X. Zhu, Direct observation of topological phonons in graphene, *Phys. Rev. Lett.* **131**, 116602 (2023).
- [22] Y. Jin, R. Wang, and H. Xu, Recipe for Dirac phonon states with a quantized valley Berry phase in two-dimensional hexagonal lattices, *Nano Lett.* **18**, 7755 (2018).
- [23] J. Li, L. Wang, J. Liu, R. Li, Z. Zhang, and X.-Q. Chen, Topological phonons in graphene, *Phys. Rev. B* **101**, 081403(R) (2020).
- [24] Z. J. Chen, R. Wang, B. W. Xia, B. B. Zheng, Y. J. Jin, Y.-J. Zhao, and H. Xu, Three-dimensional Dirac phonons with inversion symmetry, *Phys. Rev. Lett.* **126**, 185301 (2021).
- [25] Y. Feng, C. Xie, H. Chen, Y. Liu, and X. Wang, Dirac point phonons at high-symmetry points: Towards materials realization, *Phys. Rev. B* **106**, 134307 (2022).
- [26] J. Gong, J. Wang, H. Yuan, Z. Zhang, W. Wang, and X. Wang, Dirac phonons in two-dimensional materials, *Phys. Rev. B* **106**, 214317 (2022).
- [27] T. Zhang, Z. Song, A. Alexandradinata, H. Weng, C. Fang, L. Lu, and Z. Fang, Double-Weyl phonons in transition-metal monosilicides, *Phys. Rev. Lett.* **120**, 016401 (2018).
- [28] H. Miao, T. T. Zhang, L. Wang, D. Meyers, A. H. Said, Y. L. Wang, Y. G. Shi, H. M. Weng, Z. Fang, and M. P. M. Dean, Observation of double Weyl phonons in parity-breaking FeSi, *Phys. Rev. Lett.* **121**, 035302 (2018).
- [29] J. Liu, W. Hou, E. Wang, S. Zhang, J.-T. Sun, and S. Meng, Ideal type-II Weyl phonons in wurtzite CuI, *Phys. Rev. B* **100**, 081204(R) (2019).
- [30] B. W. Xia, R. Wang, Z. J. Chen, Y. J. Zhao, and H. Xu, Symmetry-protected ideal type-II Weyl phonons in CdTe, *Phys. Rev. Lett.* **123**, 065501 (2019).
- [31] T. Zhang, L. Lu, S. Murakami, Z. Fang, H. Weng, and C. Fang, Diagnosis scheme for topological degeneracies crossing high-symmetry lines, *Phys. Rev. Res.* **2**, 022066(R) (2020).
- [32] Y. J. Jin, Z. J. Chen, B. W. Xia, Y. J. Zhao, R. Wang, and H. Xu, Ideal intersecting nodal-ring phonons in bcc C<sub>8</sub>, *Phys. Rev. B* **98**, 220103(R) (2018).
- [33] T. T. Zhang, H. Miao, Q. Wang, J. Q. Lin, Y. Cao, G. Fabbris, A. H. Said, X. Liu, H. C. Lei, Z. Fang, H. M. Weng, and M. P. M. Dean, Phononic helical nodal lines with  $\mathcal{PT}$  protection in MoB<sub>2</sub>, *Phys. Rev. Lett.* **123**, 245302 (2019).
- [34] Y. Liu, N. Zou, S. Zhao, X. Chen, Y. Xu, and W. Duan, Ubiquitous topological states of phonons in solids: Silicon as a model material, *Nano Lett.* **22**, 2120 (2022).
- [35] W.-H. Dong, J. Pan, J.-T. Sun, and S. Du, Hybrid nodal surface and nodal line phonons in solids, *Phys. Rev. B* **108**, 115153 (2023).
- [36] J. Liu, P. Liu, Y. Sun, X.-Q. Chen, and J. Li, Symmetry-enforced topological phononic quadratic Dirac points, type-III nodal rings, and nodal surfaces in BaNa<sub>2</sub>, *Phys. Rev. B* **108**, 104312 (2023).
- [37] S. Park, Y. Hwang, H. C. Choi, and B.-J. Yang, Topological acoustic triple point, *Nat. Commun.* **12**, 6781 (2021).
- [38] G. F. Lange, A. Bouhon, B. Monserrat, and R.-J. Slager, Topological continuum charges of acoustic phonons in two dimensions and the Nambu-Goldstone theorem, *Phys. Rev. B* **105**, 064301 (2022).

- [39] Z.-K. Ding, Y.-J. Zeng, H. Pan, N. Luo, J. Zeng, L.-M. Tang, and K.-Q. Chen, Edge states of topological acoustic phonons in graphene zigzag nanoribbons, *Phys. Rev. B* **106**, L121401 (2022).
- [40] J. Zhu, W. Wu, J. Zhao, C. Chen, Q. Wang, X.-L. Sheng, L. Zhang, Y. X. Zhao, and S. A. Yang, Phononic real Chern insulator with protected corner modes in graphynes, *Phys. Rev. B* **105**, 085123 (2022).
- [41] M. Pan and H. Huang, Phononic Stiefel-Whitney topology with corner vibrational modes in two-dimensional Xenes and ligand-functionalized derivatives, *Phys. Rev. B* **106**, L201406 (2022).
- [42] H. Mu, B. Liu, T. Hu, and Z. Wang, Kekulé lattice in graphdiyne: Coexistence of phononic and electronic second-order topological insulator, *Nano Lett.* **22**, 1122 (2022).
- [43] F. F. Huang, P. Zhou, W. Q. Li, S. D. He, R. Tan, Z. S. Ma, and L. Z. Sun, Phononic second-order topological phase in the C<sub>3</sub>N compound, *Phys. Rev. B* **107**, 134104 (2023).
- [44] T. Zhang, T. Hu, Y. Zhang, and Z. Wang, Pseudospin polarized dual-higher-order topology in hydrogen-substituted graphdiyne, *Nano Lett.* **23**, 8319 (2023).
- [45] J. Li, Y. Liu, J. Bai, C. Xie, H. Yuan, Z. Cheng, W. Wang, X. Wang, and G. Zhang, Phononic Weyl pair, phononic Weyl complex, phononic real Chern insulator state, and phononic corner modes in 2D Kekulé-order graphene, *Appl. Phys. Rev.* **10**, 031416 (2023).
- [46] J. Zhou, Q. Wang, Q. Sun, X. S. Chen, Y. Kawazoe, and P. Jena, Ferromagnetism in semihydrogenated graphene sheet, *Nano Lett.* **9**, 3867 (2009).
- [47] G. Fiori, S. Lebègue, A. Betti, P. Michetti, M. Klintonberg, O. Eriksson, and G. Iannaccone, Simulation of hydrogenated graphene field-effect transistors through a multiscale approach, *Phys. Rev. B* **82**, 153404 (2010).
- [48] S. Demirci, T. Gorkan, E. Aktürk, and S. Ciraci, Lateral composite structures of graphene/graphane/graphone: Electronic confinement, heterostructures with tunable band alignment, and magnetic state, *J. Phys. Chem. C* **127**, 17239 (2023).
- [49] S. Rajasekaran, S. Kaya, F. Abild-Pedersen, T. Anniyev, F. Yang, D. Stacchiola, H. Ogasawara, and A. Nilsson, Reversible graphene-metal contact through hydrogenation, *Phys. Rev. B* **86**, 075417 (2012).
- [50] W. Zhao, J. Gebhardt, F. Späth, K. Gotterbarm, C. Gleichweit, H.-P. Steinrück, A. Görling, and C. Papp, Reversible hydrogenation of graphene on Ni(111)—synthesis of “graphone,” *Chem. Eur. J.* **21**, 3347 (2015).
- [51] G. Kresse and J. Furthmüller, Efficiency of *ab-initio* total energy calculations for metals and semiconductors using a plane-wave basis set, *Comput. Mater. Sci.* **6**, 15 (1996).
- [52] G. Kresse and J. Furthmüller, Efficient iterative schemes for *ab initio* total-energy calculations using a plane-wave basis set, *Phys. Rev. B* **54**, 11169 (1996).
- [53] P. Hohenberg and W. Kohn, Inhomogeneous electron gas, *Phys. Rev.* **136**, B864 (1964).
- [54] W. Kohn and L. J. Sham, Self-consistent equations including exchange and correlation effects, *Phys. Rev.* **140**, A1133 (1965).
- [55] H. J. Monkhorst and J. D. Pack, Special points for Brillouin-zone integrations, *Phys. Rev. B* **13**, 5188 (1976).
- [56] J. P. Perdew, K. Burke, and M. Ernzerhof, Generalized gradient approximation made simple, *Phys. Rev. Lett.* **77**, 3865 (1996).
- [57] A. Togo and I. Tanaka, First principles phonon calculations in materials science, *Scr. Mater.* **108**, 1 (2015).
- [58] Q.-Q. Li, W.-W. Liu, Z.-K. Ding, H. Pan, X.-H. Cao, W.-H. Xiao, N.-N. Luo, J. Zeng, L.-M. Tang, B. Li, K.-Q. Chen, and X.-D. Duan, Stacking- and strain-dependent magnetism in Janus CrSTe bilayer, *Appl. Phys. Lett.* **122**, 121902 (2023).
- [59] R. He, D. Wang, N. Luo, J. Zeng, K.-Q. Chen, and L.-M. Tang, Nonrelativistic spin-momentum coupling in antiferromagnetic twisted bilayers, *Phys. Rev. Lett.* **130**, 046401 (2023).
- [60] H. Pan, L.-M. Tang, and K.-Q. Chen, Quantum mechanical modeling of magnon-phonon scattering heat transport across three-dimensional ferromagnetic/nonmagnetic interfaces, *Phys. Rev. B* **105**, 064401 (2022).
- [61] H. Pan, Z.-K. Ding, B.-W. Zeng, N.-N. Luo, J. Zeng, L.-M. Tang, and K.-Q. Chen, *Ab initio* Boltzmann approach to coupled magnon-phonon thermal transport in ferromagnetic crystals, *Phys. Rev. B* **107**, 104303 (2023).
- [62] W.-H. Xiao, B. Zeng, Z.-K. Ding, H. Pan, W.-W. Liu, Q.-Q. Li, K. Yang, N. Luo, J. Zeng, K.-Q. Chen, and L.-M. Tang, Exceptionally high hole mobilities in monolayer group-IV monochalcogenides GeTe and SnTe, *Appl. Phys. Lett.* **123**, 013101 (2023).
- [63] X.-H. Cao, D. Wu, J. Zeng, N.-N. Luo, W.-X. Zhou, L.-M. Tang, and K.-Q. Chen, Controllable anisotropic thermoelectric properties in 2D covalent organic radical frameworks, *Appl. Phys. Lett.* **119**, 263901 (2021).
- [64] Y.-J. Zeng, Y.-X. Feng, L.-M. Tang, and K.-Q. Chen, Effect of out-of-plane strain on the phonon structures and anharmonicity of twisted multilayer graphene, *Appl. Phys. Lett.* **118**, 183103 (2021).
- [65] B. Zeng, Z.-K. Ding, H. Pan, N. Luo, J. Zeng, L.-M. Tang, and K.-Q. Chen, Strong strain-dependent phonon hydrodynamic window in bilayer graphene, *Appl. Phys. Lett.* **121**, 252202 (2022).
- [66] X. Li, C. Xia, Y. Pan, M. Gao, H. Chen, and L. Zhang, Topological chiral phonons along the line defect of intralayer heterojunctions, *Phys. Rev. B* **104**, 054103 (2021).
- [67] W. Ren, S. Lu, C. Yu, J. He, Z. Zhang, J. Chen, and G. Zhang, Impact of moiré superlattice on atomic stress and thermal transport in van der Waals heterostructures, *Appl. Phys. Rev.* **10**, 041404 (2023).
- [68] N. Li, J. Ren, L. Wang, G. Zhang, P. Hänggi, and B. Li, Colloquium: Phononics: Manipulating heat flow with electronic analogs and beyond, *Rev. Mod. Phys.* **84**, 1045 (2012).
- [69] B. Bradlyn, L. Elcoro, J. Cano, M. G. Vergniory, Z. Wang, C. Felser, M. I. Aroyo, and B. A. Bernevig, Topological quantum chemistry, *Nature (London)* **547**, 298 (2017).
- [70] J. Cano, B. Bradlyn, Z. Wang, L. Elcoro, M. G. Vergniory, C. Felser, M. I. Aroyo, and B. A. Bernevig, Building blocks of topological quantum chemistry: Elementary band representations, *Phys. Rev. B* **97**, 035139 (2018).
- [71] B. Bradlyn, L. Elcoro, M. G. Vergniory, J. Cano, Z. Wang, C. Felser, M. I. Aroyo, and B. A. Bernevig, Band connectivity for topological quantum chemistry: Band structures as a graph theory problem, *Phys. Rev. B* **97**, 035138 (2018).
- [72] M. Vergniory, L. Elcoro, C. Felser, N. Regnault, B. A. Bernevig, and Z. Wang, A complete catalogue of high-quality topological materials, *Nature (London)* **566**, 480 (2019).

- [73] Y. Xu, M. G. Vergniory, D.-S. Ma, J. L. Mañes, Z.-D. Song, B. A. Bernevig, N. Regnault, and L. Elcoro, Catalogue of topological phonon materials, [arXiv:2211.11776](https://arxiv.org/abs/2211.11776).
- [74] W. A. Benalcazar, B. A. Bernevig, and T. L. Hughes, Electric multipole moments, topological multipole moment pumping, and chiral hinge states in crystalline insulators, *Phys. Rev. B* **96**, 245115 (2017).
- [75] C. Fang, M. J. Gilbert, and B. A. Bernevig, Bulk topological invariants in noninteracting point group symmetric insulators, *Phys. Rev. B* **86**, 115112 (2012).
- [76] W. A. Benalcazar, T. Li, and T. L. Hughes, Quantization of fractional corner charge in  $C_n$ -symmetric higher-order topological crystalline insulators, *Phys. Rev. B* **99**, 245151 (2019).
- [77] See Supplemental Material at <http://link.aps.org/supplemental/10.1103/PhysRevB.109.115422> for more details about (1) gap  $\Gamma$  of the graphone phonon spectrum under different strains, (2) phonon spectra of the graphone armchair-edged nanodisks under different strains, (3) phonon spectra of the one-dimensional nanoribbons and the zero-dimensional nanodisk without the correction of the acoustic sum rule, and (4) phonon spectra of the 30 and 40 units width nanoribbons.
- [78] J. L. Mañes, Fragile phonon topology on the honeycomb lattice with time-reversal symmetry, *Phys. Rev. B* **102**, 024307 (2020).
- [79] F. Schindler, A. M. Cook, M. G. Vergniory, Z. Wang, S. S. P. Parkin, B. A. Bernevig, and T. Neupert, Higher-order topological insulators, *Sci. Adv.* **4**, eaat0346 (2018).
- [80] F. Schindler, Z. Wang, M. G. Vergniory, A. M. Cook, A. Murani, S. Sengupta, A. Y. Kasumov, R. Deblock, S. Jeon, I. Drozdov *et al.*, Higher-order topology in bismuth, *Nat. Phys.* **14**, 918 (2018).
- [81] A. Cerjan, M. Jürgensen, W. A. Benalcazar, S. Mukherjee, and M. C. Rechtsman, Observation of a higher-order topological bound state in the continuum, *Phys. Rev. Lett.* **125**, 213901 (2020).
- [82] Z. H. Li, P. Zhou, Q. H. Yan, X. Y. Peng, Z. S. Ma, and L. Z. Sun, Second-order topological insulator in two-dimensional  $C_2N$  and its derivatives, *Phys. Rev. B* **106**, 085126 (2022).
- [83] B.-B. Liu, X.-T. Zeng, C. Chen, Z. Chen, and X.-L. Sheng, Second-order and real Chern topological insulator in twisted bilayer  $\alpha$ -graphyne, *Phys. Rev. B* **106**, 035153 (2022).